UC Davis

UC Davis Previously Published Works

Title

Analysis of peristaltic waves and their role in migrating Physarum plasmodia

Permalink

https://escholarship.org/uc/item/4s0047d7

Journal

Journal of Physics D, 50(28)

ISSN

0022-3727

Authors

Lewis, Owen L

Guy, Robert D

Publication Date

2017-07-19

DOI

10.1088/1361-6463/aa76c3

Peer reviewed

eScholarship.org Powered by the California Digital Library
University of California

Analysis of Peristaltic Waves & their Role in Migrating *Physarum* Plasmodia

Owen L. Lewis[1,†] and Robert D. Guy[2]

[1]Department of Mathematics, University of Utah
[2]Department of Mathematics, University of California Davis
[†]Corresponding Author: olewis@math.utah.edu

May 18, 2017

Abstract

The true slime mold *Physarum polycephalum* exhibits a vast array of sophisticated manipulations of its intracellular cytoplasm. Growing microplasmodia of *Physarum* have been observed to adopt an elongated tadpole shape, then contract in a rhythmic, traveling wave pattern that resembles peristaltic pumping. This contraction drives a fast flow of non-gelated cytoplasm along the cell longitudinal axis. It has been hypothesized that this flow of cytoplasm is a driving factor in generating motility of the plasmodium. In this work, we use two different mathematical models to investigate how peristaltic pumping within *Physarum* may be used to drive cellular motility. We compare the relative phase of flow and deformation waves predicted by both models to similar phase data collected from *in vivo* experiments using *Physarum* plasmodia. The first is a PDE model based on a dimensional reduction of peristaltic pumping within a finite length chamber. The second is a more sophisticated computational model which accounts for more general shape changes, more complex cellular mechanics, and dynamically modulated adhesion to the underlying substrate. This models allows us to directly compute cell crawling speed. Both models suggest that a mechanical asymmetry in the cell is required to reproduce the experimental observations. Such a mechanical asymmetry is also shown to increase the potential for cellular migration, as measured by both stress generation and migration velocity.

1 Introduction

Cell migration plays a critical role in a wide variety of biological processes such as wound healing, the immune response, and morphogenesis. Amoeboid motility is a rapid type of cell migration characterized by large shape changes as the cell extends and retracts various pseudopodia and blebs [6]. Research on amoeboid motility has recently intensified in part because of a newfound appreciation of the broad applicability of amoeboid motility types. This migration mode is robust to changes in the extracellular environment and may be used to move across a surface or through a 3-D environment [7]. Recent studies have suggested that the general mechanisms of amoeboid motility may be independent of the specific molecular nature of cell-substrate adhesion [18]. Thus, amoeboid migration allows cells to move in various geometries by contracting and pushing off the surrounding environment. This work concerns a mathematical description of steaming cytoplasm in *Physarum polycephalum* microplasmodia with a particular emphasis on a mechanistic explanation on how steaming may contribute to amoeboid cell motility.

Physarum polycephalum is a slime mold that belongs to the supergroup Amoebozoa. In particular, *Physarum* belongs to the "acellular" or plasmodial slime mold subgroup. The organism is multinucleated, and a single plasmodium may grow to macroscopic length scales. Due to its large size, *Physarum* is relatively easy to study under a light microscope, and it has been used as a model organism in cellular biology for several decades. *Physarum* was heavily studied in early investigations into the nature and movement of cytoplasm [11]. Due to the prevailence of large intracellular flows, the streaming of cytoplasm within *Physarum* plasmodia has been the focus of numerous cytology studies [12, 13, 16]. In addition to simple streaming of cytoplasm, the plasmodium of physarum exhibits a vast array of cellular behaviors that have been studied in a variety of contexts. The emergence of contractile patterns has been studied in the context of coupled oscillators [26, 36, 37, 38, 39, 42] and complex viscoelastic materials [3, 27, 30, 31, 40, 41]. The branching of flow networks within physarum has even been studied as a model system of transportation networks [4, 5].

Removing a small sample of the organism results in a so-called microplasmodium. The multinucleated nature of *Physarum* means that these smaller scale plasmodia are capable of sustaining biological function and may eventually grow back to the scale of the original. Initially after segregation, microplasmodia adopt a round shape and begin to reorganize their disrupted cytoskeleton [25]. As the microplasmodia grow to a critical size (approximately 100 µm across), a sharp transition occurs [17], in which the cell develops an elongated tadpole-like shape with a flow channel of non-gelated cytoplasm along the cell longitudinal axis. An example of a microplasmodium with this elongated shape is shown in fig. 1. The anterior of the cell (right) is noticeably more spread out than the channel-like posterior (left). This structure at the "head" of the cell to lacks the well defined cytoskeletal structure of the rest of the cell [34]. In particular, the single coherent channel of non-gelated cyoplasm is not apparent at the anterior of the cell. Coincident with elongation into this tadpole shape, the plasmodium begins to exibit a drastic increase in intracellular fluid velocity, as a distinct pattern of cytoplasmic flow develops. Finally, the onset of this behavior has been observed to coincide with a drastic increase in the locomotion speed of growing plasmodia. It has naturally been hypothesized that the flow of cytoplasm is therefore a driving force in this particular example of amoeboid cell motility. To date, one study has measured the precise spatiotemporal form of the deformation of the plasmodia and the resulting flow of cytoplasm within [23]. The authors hypothesized that the relative phase of the flow and deformation waves may result in translation of the cell mass center. However, as yet, no there is no complete mechanical explanation of how this cyotplasmic flow may generate motility.

We use two distinct modeling techniques to investigate the plausibility of the description of

motility provided in [23]. First, we model a single microplasmodia as a peristaltic chamber of cytoplasmic fluid. We quantify the phase relationships between contraction and flow that necessarily result from driving cytoplasmic flow through traveling waves of contraction. These phase relationships are qualitatively compared to those observed in [23]. Simultaneously, we quantify the characteristic stresses associated with the flows predicted by our model. These stresses are found to be of a biologically relevant scale, though rather small. Second, we perform a series of simulations using a computational model of a crawling cell that allows us to explore more general mechanics and shape changes, as well as predict cell migration velocities. This computation model incorporates more complex intracellular rheology, the mechanical response of the cell membrane/cortex, and spatiotemporal variation in adhesion strength. We show that the phase relationships observed in [23] may be a product of a mechanical heterogeneity within the plasmodium, and this heterogeneity is advantageous for locomotion. In particular, mechanical heterogeneity may result in increased migration speeds.

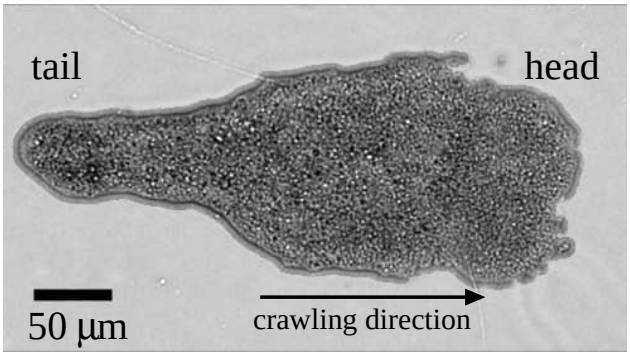

Figure 1: A typical tadpole-shaped *Physarum* microplasmodium. The anterior ("head") and posterior ("tail") are indicated, as well as the direction of migration. Image courtesy of Shun Zhang and Juan Carlos del Álamo.

2 Peristaltic Pumping in *Physarum*

In [23], the authors perform particle image velocimetry to measure the spatiotemporal flow of cytoplasm within migrating *Physarum* microplasmodia. In these experiments, the authors observe a periodic, pulsatile flow of cytoplasm forward and backward along the longitudinal axis of the plasmodium body. A region of forward flow (directed toward the anterior end of the cell) develops at the plasmodium posterior and propagates forward along the cell axis. This is followed by a region of backward flow that also develops at the posterior of the cell and propagates to the anterior. Thus, the spatiotemporal organization of the cytoplasmic flow is characterized by a *phase wave* profile. A phase wave is a profile of the form $f(kx - \omega t)$, where f is some periodic function (such as a sinusoid). For such waveforms, the wave profile will propagate through the domain with velocity ω/k. The deformation of the cell in the direction perpendicular to the longitudinal axis of the cell is also measured and shown to have a similar character. The first panel of fig. 2 is reproduced from [23]. It shows flow and deformation of the cell body as a function of time and the longitudinal cell body coordinate (called the Anterior-Posterior (AP) axis by the authors). The greyscale indicates the cross-section averaged velocity of cytoplasm along the cell axis. The pitched lines of black pixels incidate zero flow velocity and the slope of these lines may be interpreted as the phase velocity of the flow wave. The open dots indicate the onset of contraction (or local maxima of deformation).

Closed dots indicate the onset of expansion (local minima of deformation).

The pattern of traveling phase waves of both deformation and flow is characteristic of a phenomenon called peristalsis. Peristalsis is a mechanism whereby waves of contraction propagate along the exterior of a fluid-filled tube or chamber. When these waves of contraction result in net transport of fluid along the axis of the tube, it is referred to as a peristaltic pump. Peristaltic pumping is observed in numerous physiological contexts where tubular smooth muscle structures are common such as in the gastrointestinal tract, the bile ducts, and the fallopian tubes. Peristalsis also has applications in industrial processes, where a peristaltic pump can be used to move slurries and corrosive materials without the liquid coming into contact with any mechanical parts of the device. Analysis of the efficacy of peristaltic pumping is a classical problem in applied mathematics. The bulk of existing studies only consider pumping in an infinitely long domain (or approximate one using a periodic domain) [9, 10, 33]. It is not appropriate to represent a *Physarum* plasmodium as an infinitely long tube and we are not concerned with quantifying the pumping of cytoplasm from one reservoir to another. The limited studies which have considered peristaltic pumping in a finite domain are mainly concerned with mixing properties in an inertial parameter regime [32]. Other investigations have examined peristaltic contraction within *Physarum*, however the authors studied fully developed, macroscopic organisms (not microplasmodia) and were primarily concerned with efficiency of transport through a the branching network structure rather than migration [2]. As yet, no theoretical work has addressed the possibility that peristaltic motion may be utilized by a cell to "pump" itself across a substrate.

In [23], it is argued that the phase wave nature of the cytoplasmic flow is critical to generating motility via the observed behavior. This argument is motivated by two key observations. First, the direction that the phase wave travels is from the posterior to the anterior of the cell. The anterograde propogation of the flow wave is argued to result in a net forward displacement of fluid within the cell, and thus the center of mass is transported forward. This behavior is not discussed at length in the present work, but has been explored in other experimental and modeling investigations [20].

The second observation of [23] is that the flow wave is of the same period as the wave of contraction on the cell exterior. The two waves have a well-defined phase relative to one another. This can also be seen in the first panel of fig. 2. In the tail of the cell, the onset of contraction consistently precedes the maximum flow velocity by about one quarter of the period of the wave. This phase relationship is consistent throughout most of the cell. The noticeable exception to this is at the front of the cell, where the maximum flow velocity precedes the onset of expansion. To more clearly see this relationship, we extract the data gathered in [23] from the image in the first panel of fig. 2 with the goal of calculating the relative phase of the deformation wave and flow wave. At each point of the AP axis, we extract from the image the time of maximum flow velocity, as well as the time of maximum cell width. The difference between these two times, divided by the period of the wave, is interpreted as the relative phase of the two waves. This is done for three periods of the wave, and the results are presented in the second panel of fig. 2 (the cell coordinate (x) is non-dimensionalized). The black dashed line represents the averaged phase difference measured from three periods and the filled window indicates the maximum and minimum values calculated. The grey dash-dot lines highlight a phase difference of positive and negative $\pi/2$, which correspond to deformation preceding and following the flow wave respectively.

According to the authors of [23], this phase relationship ensures that forward flow of cytoplasm occurs at locations on the cell body that are (on average) wider than locations in which cytoplasm is flowing backwards. This is implies a net forward flux of material, and thus a translation of the cell. This explanation of motility is based purely on hydrodynamic phenomena and conservation of mass. It does not include any discussion of how this phase relationship may come to be, the

stresses generated by this behavior, or how those stresses may be transmitted to the substrate to enact locomotion. In this work, we address these issues with mathematical models with the aim of answering the following question: Is the observed relative phase of deformation and flow advantageous for enacting cellular motility?

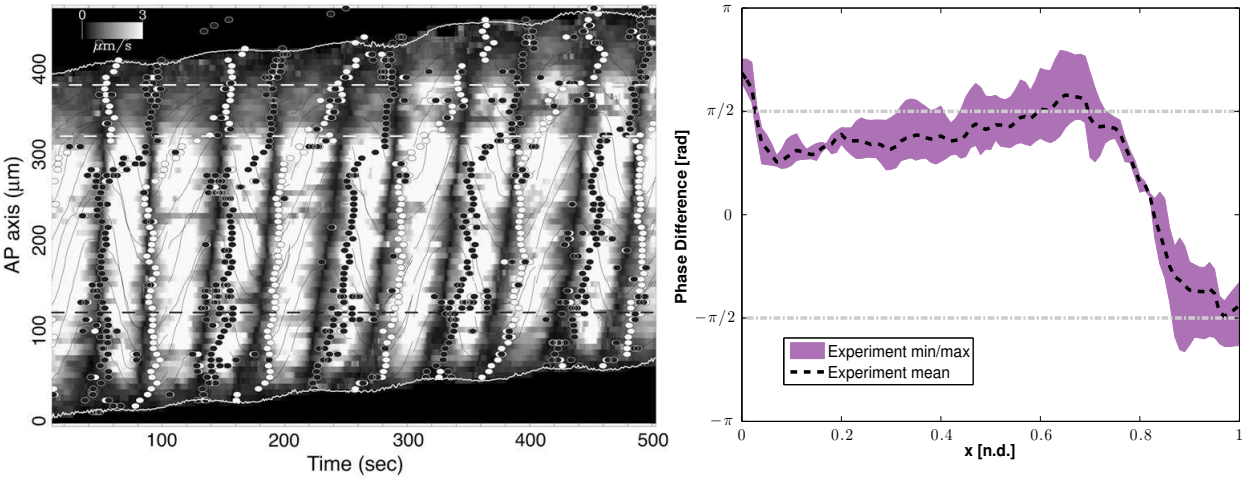

Figure 2: Left Panel: Maximum flow along the cell axis as a function of time and location on the Anterior-Posterior (AP) axis of the cell. Circles indicate temporal maxima and minima of the deformation wave. Open circles indicate maxima or "onsets of contraction," while filled circles indicate minima or "onsets of expansion." Reprinted from [23], with permission from Elsevier. Right Panel: Relative phase of the flow and deformation waves as a function of cell body coordinate (x). The space-time location of maxima and minima of the flow and deformation waves were extracted from the data in the left panel. The phase difference between the two waves was then calculated. This was performed for three full periods of the wave. Shaded region indicates the maximum and minimum of the resulting values. The black dashed line indicates the average over these three periods. The grey dash-dot lines indicate phase difference of $\pm\pi/2$ (a quarter period) for reference.

3 Analytical Model

We consider a two-dimensional flow field (in the xy-plane) of cytoplasm in a finite peristaltic chamber. In the longitudinal coordinate, the domain spans the interval $0 < x < L_x$. This domain is mean to represent the "body" of the plasmodium, but not the "head" at the anterior end. The head is mechanically distinct, and we do not wish to include it in this analysis. We discuss this point more below. In the lateral coordinate the domain is defined by the region between deformable walls described by $-h(x,t) < y < h(x,t)$ (see fig. 3). We assume that the 2-D velocity field, $\vec{u} = \langle u, v \rangle$, is incompressible (divergence-free). We let $Q(x,t)$ denote the flux of intracellular fluid through a given cross section of the cell, which is given by

$$Q(x,t) = \int_{-h}^{h} u \, dy. \tag{1}$$

To derive a constitutive equation for the flux, we integrate the incompressibility constraint in the lateral direction:

$$\begin{aligned}
0 &= \int_{-h}^{h} (u_x + v_y)\, dy \\
&= \frac{\partial}{\partial x}\int_{-h}^{h} u\, dy - \Big(u|_{y=h} - u|_{y=-h} \Big)\frac{\partial h}{\partial x} + \int_{-h}^{h} v_y\, dy \\
&\approx \frac{\partial}{\partial x}\int_{-h}^{h} u\, dy + \int_{-h}^{h} v_y\, dy \\
&= \frac{\partial}{\partial x} Q(x,t) + v|_{y=-h}^{y=h} \\
&= Q_x(x,t) + v(h(x,t),t) - v(-h(x,t),t) \\
&= Q_x(x,t) + 2h_t(x,t).
\end{aligned}$$

The resulting partial differential equation (PDE) relates the flux ($Q(x,t)$) and the chamber half width ($h(x,t)$).

$$Q_x(x,t) + 2h_t(x,t) = 0, \quad \text{for } 0 < x < L_x, \text{ and } t > 0. \tag{2}$$

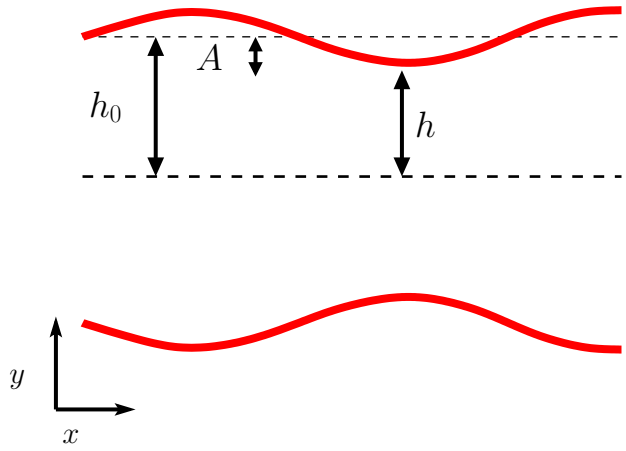

Figure 3: A schematic representation of a peristaltic chamber. The chamber wall is described by $h(x,t)$. The resting location of the wall is denoted h_0 and the amplitude of deformation from this configuration is A.

To derive this PDE, we have made several simplifying assumptions. A no slip boundary condition implies that the lateral component of fluid velocity is given by h_t and $-h_t$ at the top and bottom chamber walls. We have also assumed that $|h_x| << 1$, in order to ignore boundary terms from the Leibniz integration rule. This is equivalent to an assumption that the variation in chamber width is small compared to compared to the length of the cell. Experiments indicate that during peristaltic pumping, *Physarum* plasmodium widths vary approximately 20 µm, while the characteristic cell length may be up to 1600 µm [23, 45]. Finally, our assumption that the 2-D velocity field is incompressible is an approximation to an incompressible 3-D velocity field averaged in the z-direction. In experiments, *Physarum* are seen to change area in the xy-plane by no more than approximately 5% [45]. This implies that the planar flow field is *nearly* incompressible. Finally, we note that eq. (2) requires no assumptions about the specific rheology of the cytoplasm within the chamber. We have simply integrated the incompressibility constraint.

3.1 Chamber Deformations

We now prescribe a boundary deformation which mimics the peristaltic contractions observed to propagate down the lateral sides of migrating *Physarum* specimens. Equation (2) may then solved for the associated flux $Q(x,t)$. Experimental measurements have shown that the cell membrane deformations appear to be a phase wave, which propagates from the posterior to the anterior end of the cell [23, 45]. These wave-like contractions travel with a distinct velocity, which we refer to as the phase velocity. While the phase velocity of deformations is easily observable *in vivo*, it is not obvious what functional form best reproduces the shape of the cell boundary seen in experiments. For this reason, we will examine two idealized functional forms of the boundary deformation.

Unconstrained deformation (Open Head) First, we idealize the boundary deformation as a simple sinusoid traveling from the tail of the cell ($x = 0$) to the head of the cell ($x = 1$). The functional form of this deformation is given by

$$h(x,t) = h_0 + A\cos\left(k\frac{x}{L_x} - \omega t\right), \tag{3}$$

with the stipulation that $k \neq 0$. The parameter k is the (non-dimensional) wave number of the deformation, and the wavelength is given by $\lambda = 2\pi L_x/k$. Similarly, ω is the frequency of the wave, and the period is given by $T = 2\pi/\omega$. The ratio $\omega L_x/k$ gives the phase velocity (in units of length per time).

We make the assumption that the domain is closed at the tail ($x = 0$). Physically, this corresponds to the assumption that fluid may not pass through the cell membrane at the posterior end of the chamber. As a consequence, we impose a no flux condition ($Q(0,t) = 0$) at this end of the domain and solve eq. (2) given the boundary deformation in eq. (3). We note here that no assumptions have been made about the behavior of the model at the anterior end of the chamber ($x = L_x$). Indeed, fluid is free to flow in and out of the "head," resulting in a very clear asymmetry in the domain. We will return to this idea in the following section.

Solving eq. (2) with the given deformation and boundary condition yields the flux of fluid within the domain:

$$Q(x,t) = \frac{2AL_x\omega}{k}\left(\cos\left(k\frac{x}{L_x} - \omega t\right) - \cos(\omega t)\right). \tag{4}$$

For convenience, we define the *displacement* of the chamber wall as the difference between the chamber half-width and the average chamber half-width

$$\bar{h}(x,t) = h(x,t) - h_0 = A\cos\left(k\frac{x}{L_x} - \omega t\right). \tag{5}$$

We may regard the displacement $\bar{h}$ as the input of the model, while the resulting flux Q may be thought of as the output.

Constrained Deformation (Closed Head) We now return to the previous discussion of what boundary conditions are appropriate to impose on eq. (2). In the previous section, we have stipulated a zero flux boundary condition at the left ($x = 0$) boundary of the chamber only. This allows a free flow of fluid in and out of the right boundary ($x = L_x$). However, it is obvious that cytoplasm cannot flow freely through the anterior end of the cell membrane. We may therefore choose to impose another no flux boundary condition at the right boundary. Doing so over-determines the problem, which results in a constraint on the allowable deformations $h(x,t)$. Zero flux through

both domain boundaries implies overall volume conservation of the chamber. Thus, for the model to be solvable, the deformation must be consistent with volume conservation.

The space of deformations which satisfy this constraint is far too large to explore fully. Therefore we make the following assumption: The chamber boundary has a "preferred" deformation which is the same as in the previous section. However, there is a spatially uniform correction term which serves to impose constant volume on the chamber,

$$h(x,t) = h_0 + A\cos\left(k\frac{x}{L_x} - \omega t\right) + C(t). \tag{6}$$

A calculation shows that the correction term is given by

$$C(t) = -\frac{A}{k}\Big(\sin(k-\omega t) + \sin(\omega t)\Big). \tag{7}$$

Again, solving eq. (2) subject to the zero flux condition at the posterior end of the domain yields a complete description of the flux

$$Q(x,t) = \frac{2\omega A L_x}{k}\left(\cos\left(k\frac{x}{L_x} - \omega t\right) - \cos(\omega t)\right) + \frac{2A\omega x}{k}\big(\cos(\omega t) - \cos(k-\omega t)\big). \tag{8}$$

Notice here that evaluating the flux at the right domain endpoint gives $Q(L_x,t) = 0$. Thus, the no flux boundary condition is automatically satisfied at the right end of the domain, due to the correction imposed on the deformation h. Again, we specifically call attention to the *displacement* of the chamber wall

$$\bar{h}(x,t) = h(x,t) - h_0 = A\cos\left(k\frac{x}{L_x} - \omega t\right) - \frac{A}{k}\left(\sin(k-\omega t) + \sin(\omega t)\right), \tag{9}$$

which we regard as the input which generates an output of flux given by eq. (8).

4 Phase Calculations

We return now to the phase differences between deformation and flux shown in fig. 2. One of the goals of the model is to explain the behavior observed. The functional forms of displacement and fluid flux for both the constrained and unconstrained deformation (eqs. (4), (5), (8) and (9)) may be expressed as the real part of a complex oscillation of the form

$$\bar{h}(x,t) = \mathcal{R}e\Big[F(x,k)e^{i\omega t}\Big]$$
$$Q(x,t) = \mathcal{R}e\Big[G(x,k)e^{i\omega t}\Big].$$

We interpret the complex argument of the function $F(x,k)$ as the "phase" of the input oscillation $\bar{h}$ and the argument of $G(x,k)$ as the phase of the output oscillation Q. We compute the relative phase of the periodic displacements (eqs. (5) and (9)) with that of the periodic flux of fluid within the cell (eqs. (4) and (8)) by

$$\text{phase difference} = \text{Arg}\left[G(x,k)\right] - \text{Arg}\left[F(x,k)\right]. \tag{10}$$

Figure 4 shows phase differences predicted by the model as a function of non-dimensional body coordinate (x/L_x) for several choices of wave number k. For a given location in the cell body, a

positive phase difference implies that the flow wave precedes the deformation wave. The cell reaches its widest slightly before (temporally) the flow wave reaches its maximum. Conversely, a negative phase difference implies that the deformation wave precedes the flow wave.

In the first panel of fig. 4, we present model predictions for the case of the unconstrained deformation for several wave numbers. We present results for wave numbers $k \leq 2\pi$. This corresponds to wavelengths greater than the length of the cell body. These are the relevant wave numbers, as observations indicate the deformation wavelength may be 3 to 4 times the length of the cell [23, 45]. Regardless of the wave number of the deformation, we see a phase difference of $\pi/2$ at the posterior of the cell. This corresponds to the flow wave preceding the wave of deformation by a quarter period. Phase difference decreases as a function of cell coordinate, meaning that the deformation wave "catches up" to the flow wave as they propagate forward in the domain. The rate at which this occurs depends on wave number. Indeed, for $k \geq \pi$, (deformation wavelength twice the cell lenth) the deformation wave catches up to and eventually surpasses the flow wave. In the case $k = 2\pi$ (deformation wavelength equal to the cell body length), we see a complete reversal of the phase difference throughout the cell. While the flow wave leads by a quarter period at the posterior end of the domain, it is the deformation wave which leads by a quarter period at the anterior end.

For comparison, we present the same data for the closed head (constrained deformation) case in right panel of fig. 4. Again, the deformation wave "catches up to" the flow wave as they move to the anterior of the domain. This time, however, the behavior is a transition from $\pi/2$ to $-\pi/2$, which is symmetric about the center of the domain. Regardless of wave number, the flow wave precedes deformation in the posterior half of the domain. For smaller wave number (longer wavelength), this transition becomes sharper. Phase difference is nearly constant at $\pi/2$ in the posterior half of the domain, while it is nearly constant at $-\pi/2$ in the anterior half.

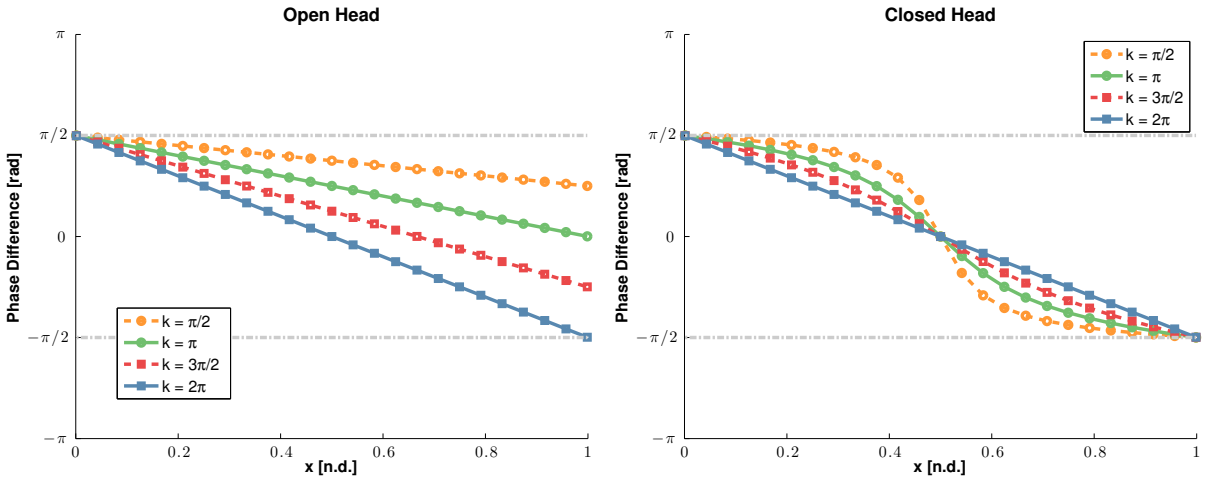

Figure 4: Phase difference as a function of cell body coordinate (x) for several wave numbers. Left panel shows results for the open head model. Right panel shows results for the closed head model. The grey dash-dot lines indicate phase difference of $\pm\pi/2$ (a quarter period) for reference.

We now focus on model predictions for wave number $k = \pi/2$, as that value corresponds to a deformation wavelength four times the length of the cell body. This wavelength agrees (roughly) with deformations observed in experiments. We compare this phase data to that observed by [23]. Figure 5 shows the model predictions for this wave number as well as the phase differences calculated from experimental data. Again, experiments show a phase difference of approximately

$\pi/2$ throughout the majority of the domain, with a sharp transition to $-\pi/2$ approximately 80% of the way from posterior to anterior. While our model reproduces aspects of this behavior, neither case we consider totally captures the phase data observed by [23].

In the case of unconstrained deformation, our model predicts a phase difference of nearly $\pi/2$ throughout the domain, with decreasing phase difference toward the anterior end of the domain. However, large scale qualitative aspects of the experimental data are missed. In particular, our model does not reproduce the sudden transition from positive to negative phase difference which occurs near the anterior end of the cell. Conversely, in the case of constrained deformation, our model does indeed predict the sudden transition in phase difference from $\pi/2$ to $-\pi/2$. However, the symmetry inherent in our model dictates that this transition occurs at the middle of the domain. Again, this fails to capture the fact that experimental data shows a relatively consistent phase difference of $\pi/2$ through a majority of the domain.

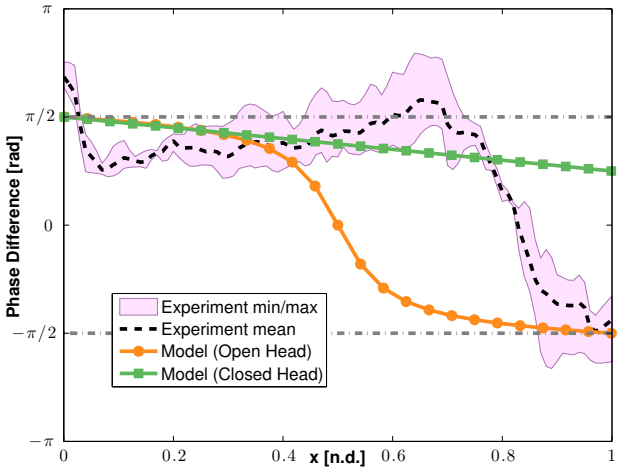

Figure 5: Phase difference predicted by model and measured experimentally as a function of cell body coordinate (x). The solid lines indicate model predictions for the open and closed head cases respectively. Shaded region and black dashed line indicate values calculated from data in fig. 2 for comparison. The grey dash-dot lines indicate phase difference of $\pm\pi/2$ (a quarter period) for reference.

Ultimately, neither case of our model results in fluid flow which captures the phase information that is reported in [23]. Indeed, it is very likely that this is due to the idealized forms of deformation which we have analyzed. The unconstrained deformation assumes that the cell body is free to pump fluid into the cell head (out the anterior end of the domain) at no penalty whatsoever. Conversely, the constrained deformation allows for no fluid to be pumped out of the anterior end of the domain. Neither of these cases faithfully describes the elastic nature of the head of *Physarum* plasmodia. This compliant structure inflates and deflates over the course of the oscillatory flow. Pumping fluid into this structure requires elastic deformation, and therefore must generate a penalty in the form of pressure acting against the flow of cytoplasm. Our two model cases may be viewed as two extreme assumptions about the compliance of this structure. The unconstrained deformation assumes infinite compliance (zero elastic modulus), while the constrained deformation assumes zero compliance (infinite elastic modulus). It seems plausible that a model incorporating finite elasticity would "interpolate" between the phasing data depcited in fig. 5 and more accurately reproduce experimental observations. We return to this idea again in Section 6.

5 Stress Generation

We turn now to a discussion the second goal of our model. In order to migrate, it is necessary for a single cell such as *Physarum* to generate stresses internally and transmit them to the underlying substrate in a coordinated fashion. Using the previously calculated expressions for flux of fluid through the cell body (eqs. (4) and (8)), we can calculate the viscous stress applied to the basal surface of the peristaltic chamber. We do not claim that viscous stress due to flow is the only mechanism by which *Physarum* plasmodia move, nor does this model attempt to describe how these stresses may be transmitted from the interior of the cell to the underlying substrate. Rather, we seek to roughly quantify the magnitude of stresses generated by the predicted fluid motion that could be utilized to enact locomotion.

The viscous stress at the basal surface of the domain can be related to the flux of fluid and deformation of the domain via the following relation (see Appendix for derivation)

$$\sigma(x,t) = \frac{3\mu}{d}\frac{Q(x,t)}{h(x,t)} = \frac{3\mu}{dh_0}\frac{Q(x,t)}{\left(1+\frac{1}{h_0}\bar{h}(x,t)\right)}, \tag{11}$$

where μ is the viscosity of the cytoplasm in the cell and d is the basal-dorsal thickness of the chamber. We now define the non-dimensional parameter

$$\varepsilon = A/h_0. \tag{12}$$

Due to the fact that $\bar{h}(x,t) \propto A$, and therefore $\frac{1}{h_0}\bar{h} \propto \varepsilon << 1$ (the nondimensional amplitude of displacement is small), the stress can be approximated using an asymptotic expansion of $\left(1+\frac{1}{h_0}\bar{h}(x,t)\right)^{-1}$

$$\sigma(x,t) \approx \frac{3\mu}{dh_0}\left(Q(x,t) - Q(x,t)\frac{\bar{h}(x,t)}{h_0}\right). \tag{13}$$

Using eq. (13), we calculate several physical quantities. The "total average stress", $\langle\overline{\sigma}\rangle$, is calculated as the average (over the whole domain, and one period of the wave $T = 2\pi/\omega$) of $\sigma(x,t)$:

$$\langle\overline{\sigma}\rangle = \frac{1}{L_x T}\int_0^T\int_0^{L_x}\frac{3\mu}{dh_0}\left(Q(x,t) - Q(x,t)\frac{\bar{h}(x,t)}{h_0}\right)dx\,dt. \tag{14}$$

Over one full period of the wave, intracellular flow generates stresses directed towards the anterior, as well as posterior end of the cell. Many of these stresses cancel each other out, and thus $\langle\overline{\sigma}\rangle$ provides a measurement of the total *unbalanced* stresses generated by the wave which may be utilized for directed motility.

We characterize the maximal scale of stresses generated by fluid flow over the course of the wave by

$$\overline{\sigma}_{\max} = \max_{t\in[0,T]}\left(\frac{1}{L_x}\int_0^{L_x}\frac{3\mu}{h_0 d}Q(x,t)\,dx\right). \tag{15}$$

We refer to the quantity $\overline{\sigma}_{\max}$ as the "maximal stress" (a slight abuse of nomenclature). Because the nondimensional amplitude of displacement is small, the second term in eq. (13) is small compared to the first. Therefore eq. (15) provides a good approximation to the maximal magnitude of stress generated over the course of one period by only considering the first term.

Finally, we define the quantity R as the ratio of the "total average stress" to the "maximal stress"

$$R = \frac{\langle\overline{\sigma}\rangle}{\overline{\sigma}_{\max}}.$$

If $\overline{\sigma}_{\max}$ quantifies the approximate scale of stresses generated by the flow wave, then R represents the proportion of stresses that are not canceled over one full period and may be utilized to generate directed motility. After the necessary calculations, we can express the three quantities of interest as

$$\overline{\sigma}_{\max} = \Sigma\varepsilon f(k), \tag{16}$$

$$\langle\overline{\sigma}\rangle = \Sigma\varepsilon^2 g(k), \tag{17}$$

$$R = \varepsilon r(k), \tag{18}$$

where the functions f, g, and r depend only on the wave number (k) of the imposed deformation. The characteristic stress scale of the problem is given by

$$\Sigma = \frac{3\mu\omega L_x}{d}. \tag{19}$$

Figure 6 shows normalized stress measurements (total average, maximum, and ratio) for both the open head (unconstrained) and closed head (constrained) deformations.

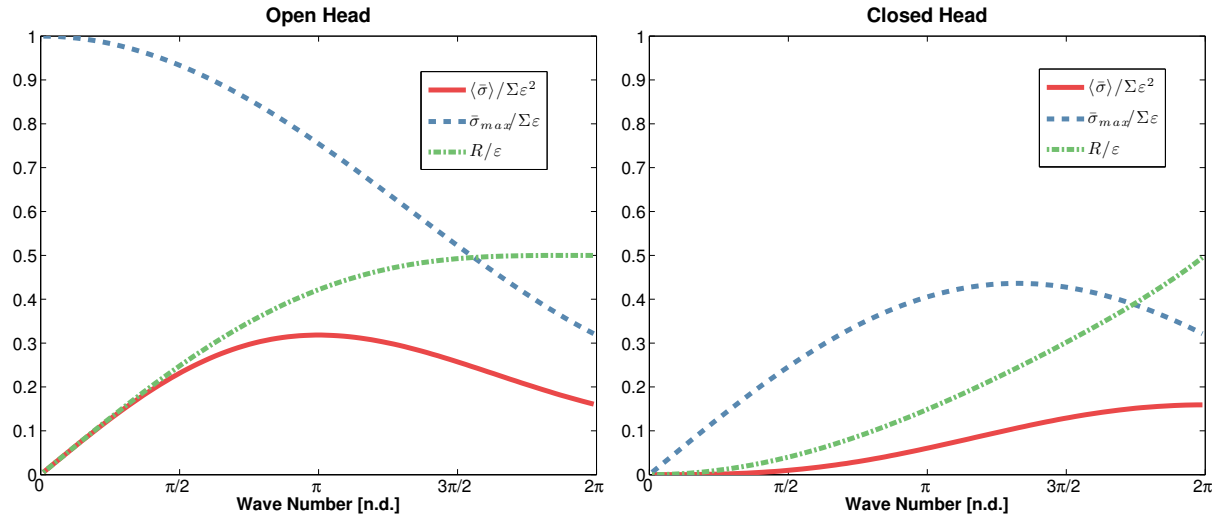

Figure 6: Normalized stresses associated with peristaltic pumping for the open and closed head cases. Total average stress is indicated with a solid red line. Maximum average stress is indicated with blue dashed line. The ratio of average to maximum is indicated with a green dash-dot line.

Figure 6 reveals two immediate trends. For all values of wave number considered, both maximum stress and the ratio of stresses are greater in the case of the unconstrained deformation than the case of constrained deformation. This implies that the asymmetry imposed by allowing fluid to flow out of the anterior end of the domain increases the characteristic magnitude of stresses generated. However, it *also* results in a larger percentage of those stresses remaining after one full period of the wave. If we consider only wave number $k = \pi/2$ (which corresponds to deformations seen in experiments), we can evaluate $\overline{\sigma}_{\max}$, $\langle\overline{\sigma}\rangle$ and R. Doing so results in the values listed in table 1. For parameter values used to calculate Σ, see table A.1 in the appendix. Again, we see the same trend. The unconstrained deformation increases the maximum stress generated by nearly a factor of four relative to the constrained deformation. It also increases ratio R approximately 6 fold, and the

average directed stresses generated over one period of the wave ($\langle\overline{\sigma}\rangle$) are increased by approximately a factor of 24. Thus, it appears that the asymmetry of the domain drastically increases the ability of the cell to generate directed stresses which could hypothetically aid in locomotion.

Table 1: Basal viscous stresses associated with flow. All values calculated with $k = \pi/2$.

		Constrained deformation	Unconstrained deformation
$\overline{\sigma}_{\max}$	Maximum Average Stress	0.6150 Pa	2.333 Pa
$\langle\overline{\sigma}\rangle$	Total Average Stress	0.006159 Pa	0.1446 Pa
$\langle\overline{\sigma}\rangle/\overline{\sigma}_{\max}$	Ratio Of Stresses	0.01001	0.06198

6 Simulation of Crawling Cells

Stress calculations in section 5 indicate that allowing fluid to flow through the anterior end of the domain is advantageous to stress generation, and potentially to enacting motility. However, the phase calculations from section 4 indicate that pumping fluid freely through the anterior of the cell domain does a poor job of reproducing the relative phase data observed in experiments. Conversely, a domain with a "closed" head seems to capture more of the qualitative aspects of the experimental data, but predicts drastically reduced stress generation, and by implication, drastically reduced capacity to enact motility. Of course, the body of *Physarum* plasmodia are not perfectly described by a peristaltic chamber with an open, or closed, head. *In vivo*, the plasmodium body gives way to a compliant, structure that is mechanically distinct from the majority of the cell body, with a much less well defined cytoskeleton [34]. As constructed, our model is incapable of accounting for the elastic properties of the body, and so we use a computational model to to explore the role of mechanical heterogeneity.

6.1 Numerical Model

Following our previous work in [20], we model a crawling *Physarum* plasmodium as an actively contractile poroelastic medium surrounded by an impermeable lipid membrane, and adherent to the substrate via dynamically modulated visco-elastic interactions. Figure 7 shows a cartoon depiction of the relevant structures in the model. The cell interior volume is filled with incompressible Newtonian fluid (which is depicted by the shaded region). The fluid permeates a zero-volume, porous, neo-hookean elastic material (representing the cytoskeleton of the cell) which is depicted as a network of red circles connected with dashed edges. The exterior boundary of the cytoskeletal network is connected to an elastic membrane that is impermeable to the interstitial fluid (depicted by blue diamonds connected with thicker dashed edges). Finally, each point of the cytoskeletal network is connected to a corresponding adhesive point (depicted as brown x's) via a hookean elastic linkage (solid pink edges).

We estimate an upper bound on the Reynolds number of cytoplasmic flow in *Physarum* by using a characteristic length scale equal to the cell length ($L \approx 400$ µm), a characteristic velocity take from the experiments of [23] ($U \approx 5$ µm/sec), and the kinematic viscosity of water ($\nu \approx 10^{-6}$ m^2/sec). Doing so results in a Reynolds number of

$$\mathrm{Re} = \frac{UL}{\nu} \approx 2 \times 10^{-3}. \tag{20}$$

This calculation likely underestimates the viscosity of cytosol by a large margin. Therefore, we can safely regard this as an upper limit for the Reynolds number of cytoplasmic flow, and conclude that

inertial effects are negligible. For this reasons the equations governing the motion of cytoplasm are the Stokes forced equation.

$$\mu\Delta\vec{u} - \nabla p + \vec{f}_{\text{drag}} + \vec{f}_{\text{memb}} = 0, \tag{21}$$

$$\nabla \cdot \vec{u} = 0. \tag{22}$$

Here, $\vec{f}_{\text{memb}}$ is a singular force applied to the intracellular fluid by the cell membrane, and is composed of internal elastic forces, surface tension, and elastic attachment to the internal cytoskeleton. The term $\vec{f}_{\text{drag}}$ is the body force of drag due to relative motion of fluid and cytoskeleton. The equation that governs the movement of the internal cytoskeleton is

$$\vec{f}_{\text{elas}} + \vec{f}_{\text{act}} + \vec{f}_{\text{memb/cyt}} + \vec{f}_{\text{adh}} - \vec{f}_{\text{drag}} = 0. \tag{23}$$

The term $\vec{f}_{\text{elas}}$ is the passive elastic force within the cytoskeleton due to deformation, $\vec{f}_{\text{act}}$ is a prescribed active contractile force within the cytoskeleton, $\vec{f}_{\text{memb/cyt}}$ is an elastic force generated by relative motion of the membrane and boundary of the cytoskeleton, and $\vec{f}_{\text{adh}}$ is an elastic force generated by relative motion of the cytoskeleton and the associated adhesive complexes. Finally, the equation governing the motion of adhesive complexes relative to the substrate is

$$\vec{f}_{\text{subs}} - \vec{f}_{\text{adh}} = 0. \tag{24}$$

Here, $\vec{f}_{\text{subs}}$ is a viscous force generated by relative motion of the adhesive complexes and the fixed substrate. Constitutive relations for these forces, parameter values used, as well as specifics of the discretization and simulation of these equations can be found in the Appendix and our previous work [20, 35].

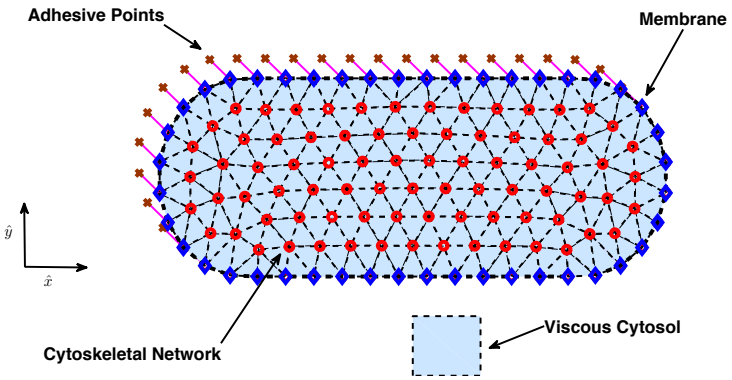

Figure 7: A schematic representation of a model crawling cell. The cell membrane is indicated with blue diamonds. The poroelastic cell interior is indicated with red circles connected with black dashed edges, while the interstitial fluid is depicted with blue shading. Adhesive points are indicated with brown x's, and connected to the elastic interior via pink edges.

This modeling framework provides two major advantages over the analytical model from section 3. Because the model explicitly incorporates adhesion of the plasmodium to the underlying substrate, we are able to capture actual crawling speeds of the cell, as opposed to simply quantifying

stresses that *might* contribute to crawling. Material points within the cell move in the lab frame, and their velocity/position is an output of the simulation. Additionally, it provides direct control over the mechanical properties of the cell domain in a spatially heterogeneous manner, allowing us to create a more elastically compliant "head" at the anterior end of the cell. We choose the point 80% of the distance from the posterior to the anterior end of the cell. This is our line of delineation between the "head" and "tail." We then set all elastic parameters in the head to be some fixed proportion of the corresponding elastic parameters in the tail. This proportion is referred to as the "scale factor" and is denoted s. A scale factor of $s = 1$ represents a mechanically hemogeneous cell, while a scale factor of $s = 1/2$ corresponds to a head which is twice as compliant as the tail.

The model is driven with a periodic traveling wave of contractile stress within the cytoskeleton. This contractile stress is again a simple sinusoid propagating from tail to head with period and phase velocity chosen to reproduce observed behavior from [23]. The functional form of the contraction is given by

$$\sigma_{\text{cont}} = \frac{A_{\text{stress}}}{2}\left(1 + \sin\Big(kx - \omega t\Big)\right), \tag{25}$$

where x is the non-dimensional longitudinal cell body coordinate. The value $x = 0$ corresponds to the tail of the cell, while $x = 1$ is the head. We represent the dynamics of adhesion to the underlying substrate via a viscous drag law. The force $\vec{f}_{\text{subs}}$ is of the form

$$\vec{f}_{\text{subs}} = -\zeta(x,t)\vec{u}_{\text{adh}}, \tag{26}$$

where $\vec{u}_{\text{adh}}$ is the velocity of the adhesion complexes (relative to the substrate), and ζ is a viscous interaction coefficient. As in our previous work in [20], we investigate an idealized ζ of the form

$$\zeta(x,t) = \frac{A_{\text{adh}}}{2}\left(1 + \cos\Big(kx - \omega t + \phi\Big)\right) + \epsilon. \tag{27}$$

The wavelength and period of the adhesion modulation are assumed to be the same as those of the contractile wave. The parameter ϕ represents the phase of the coordinated adhesion relative to the wave of contraction strength (eq. (25)). The amplitude parameter A_{adh} is a measure of the strength of active coordinated adhesion. The parameter ϵ represents non-specific adhesive interactions between the substrate and the basal surface of the cell. We report the strength of coordinated adhesion in non-dimensional units of $[A_{\text{adh}}/\epsilon]$.

6.2 Phase Calculations

Simulations are performed with parameters listed in table A.3 and last for three full periods of the wave. The resulting velocity field $\vec{u}$ is averaged over each cross section of the cell to generate kymographs. Figure 8 shows flow kymographs generated by our simulations with scale factors $s = 1$, $s = 3/4$ and $s = 1/2$. The colormap indicates the averaged flow velocity in the longitudinal direction as a function of time and cell body coordinate. The markers overlaying the colormap indicate the time at which each cross section is at its widest (white) and narrowest (black). The flow wave patterns depicted are qualitatively similar to those measured *in vivo* and illustrated in fig. 2. However, the lines which depict the propagation of the deformation waves in fig. 8 are visually distinct from each other. In all cases, the deformation wave precedes the flow wave by approximately a quarter period at the posterior of the cell (cell coordinate $x = 0$), and follows the flow wave by about a quarter period at the anterior of the cell (cell coordinate $x = 1$). However, the location of the transition has an obvious dependence on scale factor. For scale factor $s = 1$,

we see the transition occur at nearly the center of the cell. As the scale factor is decreased, the qualitative shape of the transition changes slightly, but the location unmistakably shifts toward the anterior of the cell. This more closely reproduces the trend seen in the data reported [23].

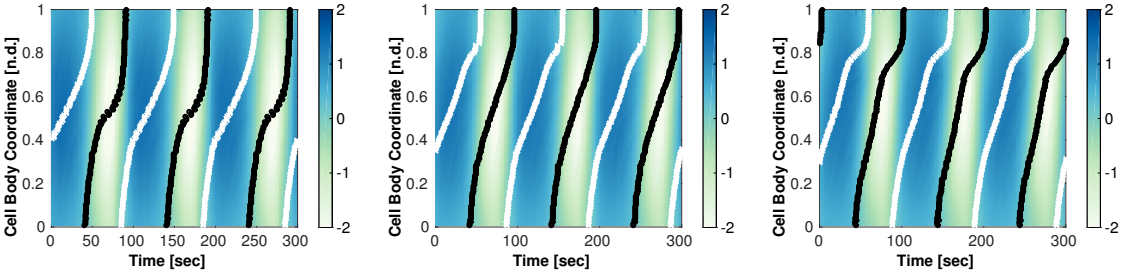

(a) Scale Factor = 1. (b) Scale Factor = 3/4. (c) Scale Factor = 1/2.

Figure 8: Cross section averaged intracellular flow velocity and cell boundary deformation. The colormap indicates average flow component along the cell longitudinal axis ([µm/sec]) as a function of time ([sec]) and cell longitudinal coordinate ([n.d.]). The black lines indicate maximum cell width, or the onset of contraction. The white lines indicated minimum cell width, or the onset of expansion.

To more clearly illustrate this concept we extract the relative phase of flow and deformation waves from our simulations and compare them to the phase extracted from fig. 2. The results of this comparison are shown in fig. 9. The graph clearly illustrates the transition from positive to negative phase difference shifting toward the front of the cell as the compliance of the head is increased (decreasing scale factor). Consequently, larger portions of the cell domain exhibit positive phase difference. In both respects, a more compliant head results in a more faithful reproduction of the phase data extracted from the experiments of [23].

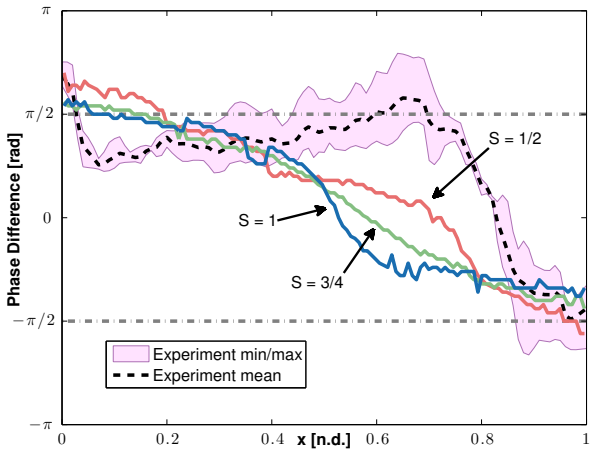

Figure 9: The solid lines indicate the phase difference predicted by our numerical model for three values of scale factor. Shaded region and black dashed line indicate values calculated from data in fig. 2 for comparison. The grey dash-dot lines indicate phase difference of $\pm\pi/2$ (a quarter period) for reference.

6.3 Stress Calculations

We now address the actual stresses our numerical model applies to the substrate and the emergent migration speed of the cell. One of the quantities calculated during simulation of our numerical model is the stress applied to the underlying substrate $\sigma^s(x_{\text{lab}}, y_{\text{lab}}, t)$. Here, the superscript "s" is meant to denote "from simulation," while the subscript "lab" indicates lab coordinates (as opposed to cell body coordinates). From this we can calculate the spatial mean $\overline{\sigma}^s(t)$. Finally, we calculate the "total average" stress $\langle\overline{\sigma}^s\rangle$ by taking the mean in time, as well as the "maximum stress" $\overline{\sigma}^s_{\max}$ by taking the maximal value over the duration of the simulation.

The calculated values of $\langle\overline{\sigma}^s\rangle$, $\overline{\sigma}^s_{\max}$ and their ratio, are shown in table 2. When we compare these values to those calculated from our analytical model (table 1), some similarities are immediately evident. The values calculated for maximum and total average stress are of roughly the same scale as those predicted by the analytical model. It is not immediately obvious that this should be the case, as our analytical model only quantified the characteristic scale of viscous stresses associated with the peristaltic flow and made no attempt to model how they may be transmitted to the substrate. Conversely our numerical model calculates the *actual* stresses applied to the substrate by a migrating model cell. The general agreement between these two models may be interpreted as a validation of the approach we adopt in section 5. The one exception to this statement is that in the case of the constrained deformation (closed head), the analytical model predicts total average stresses nearly two orders of magnitude smaller. This is likely due to the the fact that in the computational model, the cell body has an elastic response which gives an additional asymmetry not present in the analytical model.

Table 2: Stresses applied to substrate in simulated crawling cells

		Scale Factor = 1	Scale Factor = 3/4	Scale Factor = 1/2
$\overline{\sigma}^s_{\max}$	Maximum Average Stress	1.2218 Pa	1.2857 Pa	1.5737 Pa
$\langle\overline{\sigma}^s\rangle$	Total Average Stress	0.4043 Pa	0.5497 Pa	0.7148 Pa
$\langle\overline{\sigma}^s\rangle/\overline{\sigma}^s_{\max}$	Ratio Of Stresses	0.3309	0.4276	0.4542

Another trend immediately apparent is that as the scale factor decreases and the cell head becomes more compliant, stress generation is improved. Not only does maximum stress increase as the cell becomes more mechanically asymmetric, but so does the ratio of total average to maximum stress. This means that a mechanically asymmetric cell generates larger characteristic stresses, and a larger proportion of them remain uncanceled after a full period of the wave. Comparing scale factor $s = 1$ to $s = 1/2$, we see that while maximum stress increases by approximately 30%, the total average stress increases by nearly 100%. Again, this trend mirrors the predictions of the analytical model in section 5.

6.4 Crawling Speed

Finally, one of the measurable outputs of our numerical model is the actual migration speed of the model cell. In [20] we showed that two aspects of adhesion were critical to generating motility. Both the strength (quantified by A_{adh}) and the coordination relative to the driving contraction (quantified by ϕ) have a profound impact on migration. For $\phi = 3\pi/2$ the numerical model predicts robust migration speeds over a wide range of values of adhesive interaction (discussed at length in [20]). In the limit that the cell is weekly or strongly adherent, the migration speed decreases to negligible

values, and the coordination parameter ϕ does not matter. For this reason, we only present data for $\phi = 3\pi/2$ and moderate values of adhesion here.

Figure 10 shows the computed crawling speed of the cell for the three considered scale factors over a wide range of adhesion strengths. The figure shows that, generically, decreasing scale factor (more compliant cell head) corresponds to increased migration speed. This is true for nearly all parameter values. For moderately adherent cells that exhibit fast migration speeds, scale factor $s = 1/2$ results in as much as a 70% increase in migration speed. Again, it appears that the mechanical asymmetry (decreased scale factor) is advantageous for generating motility.

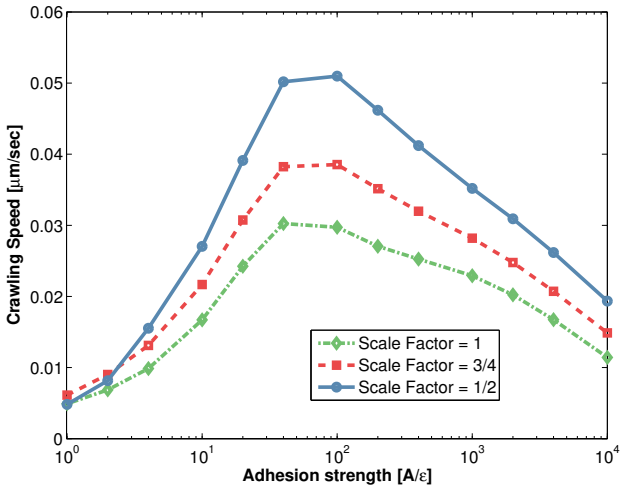

Figure 10: Crawling speed of model cell ([µm/sec]) as a function of adhesion strength and scale factor.

7 Discussion

Small *Physarum* plasmodia exhibit peristaltic contractions of the cell membrane and a periodic streaming flow of cytoplasm as they migrate [20, 23, 46], and these flows have been postulated to be responsible for driving the motility [23]. We developed a simplified mathematical model that treats the migrating *Physarum* plasmodium as a peristaltic chamber to explore the phase relationship between flow and deformation and its role in motility. The model results reproduce certain aspects of the observed phase relationship, and they strongly suggest that a mechanical asymmetry in the form of a softer anterior is required to reproduce experimental observations. To further explore the role a mechanically distinct head may play in generating the phase data reported in [23], we used a computational model of a crawling cell. As the cell head is softened, the model predicts phase data similar to those reported in [23] and the crawling speed increases.

We note here that the relative phases calculated from our two models are dissimilar in several respects (even when comparing the "closed head" case of the first model to the numerical model with scale factor 1). The differences in the models' behavior is not surprising given that the analytical model is driven by imposing a deformation, while the numerical model is driven by imposing a wave of contractile stress. This is an important distinction, as the resulting deformation achieved depends on the overall rheology of the model cell. In this respect, the numerical model is more like the actual organism. *Physarum* produces the observed deformations by contracting the actin-myosin cytoskeleton in a periodic fashion.

Contraction waves within *Physarum* are the result of calcium oscillations which likely depend on regulatory and signaling pathways that are not well studied. Data on the contractile stress has not been reported, and measuring the calcium oscillations is a problem which is the subject of ongoing investigation [46]. In the computational model the traveling sinusoidal contraction wave eq. (25) was selected for simplicity. The period and wavelength were assumed to be the same as the flow wave, and the strength was chosen to give deformations of approximately the amplitude reported in [23]. The computational model qualitatively captures the observed phase relationships between flow and deformation, and the results of this investigation would not be altered in any substantive manner if the form of contraction was "tuned" to give deformations which more precisely match experiments.

A major result of both models is the conclusion that introducing mechanical heterogeneity (either by allowing unconstrained deformations that pump fluid into the head, or by softening the elastic response of the cell anterior) not only affects the measured phase data, but actually increases the ability for the cell to migrate. The characteristic scale of stresses generated increases when asymmetry is introduced, as does the proportion of stresses which are directed, and not "canceled out" over one period of the oscillation. In the case of our numerical model, we actually see a drastic increase in migration velocity as the head is softened. However, this does not necessarily imply that the flow/deformation relationship itself is responsible for motility.

In [20] we used the same numerical model used here to investigate the relationship that adhesion has on migrating *Physarum* plasmodia. One conclusion of that work was that the coordination of adhesion strength is a dominant factor determining locomotion. Indeed, cells driven by the same contraction, and exhibiting nearly identical deformation and flow waves, could be made to migrate in different directions depending on how the spatiotemporal form of adhesion was modulated. Given this, it is possible that the flow waves observed in [23] and reproduced in this work are not directly responsible for driving migration. Rather, the fluid may play a role in establishing the long-range coordination of contraction and adhesion that is necessary for migration by transporting calcium or other chemical signals and propagating mechanical signals via hydrodynamic pressure.

Acknowledgments

The authors would like to thank Shun Zhang, Juan Carlos del Álamo, and Toshiyuki Nakagaki for image data and for helpful discussions related to this work. The work of O. Lewis was partially supported by NSF grant DMS-RTG 1148230.

References

[1] D J Acheson. *Elementary Fluid Dynamics*. Oxford Applied Mathematics and Computing Science Series. The Clarendon Press, Oxford University Press, New York, 1990.

[2] Karen Alim, Gabriel Amselem, François Peaudecerf, Michael P Brenner, and Anne Pringle. Random Network Peristalsis in Physarum Polycephalum Organizes Fluid Flows Across an Individual. *Proceedings of the National Academy of Sciences of the United States of America*, 110(33):13306–13311, August 2013.

[3] Sergio Alonso, Ulrike Strachauer, Markus Radszuweit, Markus Bär, and Marcus J B Hauser. Oscillations and Uniaxial Mechanochemical Waves in a Model of an Active Poroelastic Medium: Application to Deformation Patterns in Protoplasmic Droplets of Physarum Polycephalum. *Physica D: Nonlinear Phenomena*, 318:58–69, April 2016.

[4] Werner Baumgarten and Marcus J B Hauser. Functional Organization of the Vascular Network of Physarum polycephalum. *Physical Biology*, 10(2):026003–026003, April 2013.

[5] Werner Baumgarten, Tetsuo Ueda, and Marcus J B Hauser. Plasmodial Vein Networks of the Slime Mold Physarum polycephalum Form Regular Graphs. *Physical Review E*, 82(4):046113–046113, October 2010.

[6] D Bray. *Cell Movements*. From Molecules to Motility. Garland, New York, 2001.

[7] Guillaume Charras and Ewa Paluch. Blebs Lead the Way: How to Migrate Without Lamellipodia. *Nature Reviews: Molecular Cell Biology*, 9(9):730–736, September 2008.

[8] Guillaume T Charras, Justin C Yarrow, Mike A Horton, L Mahadevan, and T J Mitchison. Non-Equilibration of Hydrostatic Pressure in Blebbing Cells. *Nature*, 435(7040):365–369, May 2005.

[9] Y C Fung and C S Yih. Peristaltic Transport. *Journal of Applied Mechanics*, 35(4):669–675, 1968.

[10] M Y Jaffrin and A H Shapiro. Peristaltic Pumping. *Annual Review of Fluid Mechanics*, 3:13–37, 1971.

[11] N Kamiya. Protoplasmic Streaming. *Protoplasmatologia*, VIII, 1959.

[12] N Kamiya. Protoplasmic Streaming. *Protoplasma*, 53:600–614, 1961.

[13] N Kamiya. The Mechanism of Cytoplasmic Movement in a Myxomycete Plasmodium. *Symposia of the Society for Experimental Biology*, 22:199–214, 1968.

[14] N Kamiya, S Abe, and H Nakajima. Simultaneous Measurement of Respiration and the Motive Force of Protoplasmic Streaming in the Myxomycete Plasmodium. *Proceedings of the Japan Academy*, 33:206–210, 1957.

[15] Kinneret Keren, Patricia T Yam, Anika Kinkhabwala, Alex Mogilner, and Julie A Theriot. Intracellular Fluid Flow in Rapidly Moving Cells. *Nature Cell Biology*, 11(10):1219–1224, October 2009.

[16] Dietrich Kessler. Plasmodial Structure and Motility. In Henery Aldrich, editor, *Cell Biology of Physarum and Didymium*, pages 145–208. New York, 1982.

[17] S Koya and T Ueda. The Onset of Rhythmic Streaming in the Physarum Plasmodium. *ACH, Models in Chemistry*, 135(3):297–304, 1998.

[18] Tim Lämmermann, Bernhard L Bader, Susan J Monkley, Tim Worbs, Roland Wedlich-Söldner, Karin Hirsch, Markus Keller, Reinhold Förster, David R Critchley, Reinhard Fässler, and Michael Sixt. Rapid Leukocyte Migration by Integrin-Independent Flowing and Squeezing. *Nature*, 453(7191):51–55, May 2008.

[19] Owen L Lewis. *Mathematical Investigation of Hydrodynamic Contributions to Amoeboid Cell Motility in Physarum polycephalum.* PhD thesis, University of California Davis, December 2014.

[20] Owen L Lewis, Shun Zhang, Robert D Guy, and Juan C Del Alamo. Coordination of contractility, adhesion and flow in migrating Physarum amoebae. *Journal of the Royal Society Interface*, 12(106), May 2015.

[21] C T Lim, E H Zhou, and S T Quek. Mechanical Models for Living Cells–a Review. *Journal of Biomechanics*, 39(2):195–216, 2006.

[22] K Luby-Phelps. Physical Properties of Cytoplasm. *Current Opinion in Cell Biology*, 6(1):3–9, February 1994.

[23] Kenji Matsumoto, Seiji Takagi, and Toshiyuki Nakagaki. Locomotive Mechanism of Physarum Plasmodia Based on Spatiotemporal Analysis of Protoplasmic Streaming. *Biophysical Journal*, 94(7):2492–2504, April 2008.

[24] Rajat Mittal and Gianluca Iaccarino. Immersed Boundary Methods. *Annual Review of Fluid Mechanics*, 37(1):239–261, January 2005.

[25] R Nagai and T Kato. Cytoplasmic Filaments and Their Assembly Into Bundles in Physarum Plasmodium. *Protoplasma*, 86:141–158, 1975.

[26] Toshiyuki Nakagaki, Hiroyasu Yamada, and Masami Ito. Reaction–Diffusion–Advection Model for Pattern Formation of Rhythmic Contraction in a Giant Amoeboid Cell of the Physarum Plasmodium. *Journal of Theoretical Biology*, 197:497–506, March 1999.

[27] George F Oster and G M Odell. Mechanics of Cytogels I: Oscillations in Physarum. *Cell Motility*, 4:469–503, October 1984.

[28] Charles S Peskin. Numerical Analysis of Blood Flow in the Heart. *Journal of Computational Physics*, 25(3):220–252, November 1977.

[29] JLM Poiseuille. Experimental Research on the Movement of Liquids in Tubes of Very Small Diameters. *Mémoires presentés par divers savants a lAcadémie Royale des Sciences de lInstitut de France*, 9:433–544, 1846.

[30] Markus Radszuweit, Sergio Alonso, Harald Engel, and Markus Bär. Intracellular Mechanochemical Waves in an Active Poroelastic Model. *Physical Review Letters*, 110(13):138102, 2013.

[31] Markus Radszuweit, Harald Engel, and Markus Bär. An Active Poroelastic Model for Mechanochemical Patterns in Protoplasmic Droplets of Physarum polycephalum. *PLoS ONE*, 9(6):e99220, 2014.

[32] Kiril P Selverov and H A Stone. Peristaltically Driven Channel Flows with Applications Toward Micromixing. *Physics of Fluids*, 13(7):1837–1859, July 2001.

[33] A H Shapiro, M Y Jaffrin, and S L Weinberg. Peristaltic Pumping with Long Wavelengths at Low Reynolds Number. *Journal of Fluid Mechanics*, 37(4):799–825, July 1969.

[34] W Stockem and K Brix. Analysis of Microfilament Organization and Contractile Activities in Physarum. *International Review of Cytology - A Survey of Cell Biology*, 149:145–215, 1994.

[35] W Strychalski, C A Copos, O L Lewis, and R D Guy. A Poroelastic Immersed Boundary Method with Applications to Cell Biology. *Journal of Computational Physics*, 282:77–97, 2014.

[36] Kengo Takahashi, Go Uchida, Zi-Song Hu, and Yoshimi Tsuchiya. Entrainment of the Self-Sustained Oscillation in a Physarum polycephalum Strand as a One-Dimensionally Coupled Oscillator System. *Journal of Theoretical Biology*, 184(2):105–110, January 1997.

[37] A Takamatsu, T Fujii, and I Endo. Time Delay Effect in a Living Coupled Oscillator System with the Plasmodium of Physarum polycephalum. *Physical Review Letters*, 85(9):2026–2029, August 2000.

[38] A Takamatsu, R Tanaka, H Yamada, Toshiyuki Nakagaki, T Fujii, and I Endo. Spatiotemporal Symmetry in Rings of Coupled Biological Oscillators of Physarum Plasmodial Slime Mold. *Physical Review Letters*, 87(7):078102, August 2001.

[39] Atsuko Takamatsu, Kengo Takahashi, Makoto Nagao, and Yoshimi Tsuchiya. Frequency Coupling Model for Dynamics of Responses to Stimuli in Plasmodium of Physarum polycephalum. *Journal of the Physical Society of Japan*, 66(6):1638–1646, June 1997.

[40] V A Teplov, Yu M Romanovsky, and O A Latushkin. A Continuum Model of Contraction Waves and Protoplasm Streaming in Strands of Physarum Plasmodium. *BioSystems*, 24:269–289, July 1991.

[41] Vladimir A Teplov, Yuri M Romanovsky, Dmitri A Pavlov, and Wolfgang Alt. Auto-oscillatory Processes and Feedback Mechanisms in Physarum Plasmodium Motility. In *Dynamics of Cell and Tissue Motion*, pages 83–92. Birkhäuser Basel, Basel, January 1997.

[42] A Tero, R Kobayashi, and Toshiyuki Nakagaki. A Coupled-Oscillator Model with a Conservation Law for the Rhythmic Amoeboid Movements of Plasmodial Slime Molds. *Physica D: Nonlinear Phenomena*, 205(1-4):125–135, 2005.

[43] O Thoumine, O Cardoso, and J J Meister. Changes in the Mechanical Properties of Fibroblasts During Spreading: a Micromanipulation Study. *European Biophysics Journal*, 28(3):222–234, 1999.

[44] Jean-Yves Tinevez, Ulrike Schulze, Guillaume Salbreux, Julia Roensch, Jean François Joanny, and Ewa Paluch. Role of cortical tension in bleb growth. *Proceedings of the National Academy of Sciences of the United States of America*, 106(44):18581–18586, November 2009.

[45] Shun Zhang. Personal Communication. December 2013.

[46] Shun Zhang, Robert D Guy, Juan C Lasheras, and Juan C Del Àlamo. Self-organized mechanochemical dynamics in amoeboid locomotion of Physarum fragments. *Journal of Physics D: Applied Physics*, Accepted.

A Appendix

A.1 Analytical Model Details

A.1.1 Calculating Viscous Stress

Figure A.1 shows an illustrative example of a 3-dimensional peristaltic chamber filled with fluid. Within the chamber, we assume that inertial effects are negligible, and therefore the force density balance on the fluid is given by Stokes equations:

$$\mu \Delta \vec{u} - \nabla p = 0, \tag{A.1}$$

$$\nabla \cdot \vec{u} = 0. \tag{A.2}$$

Here $\vec{u} = \langle u, v, w \rangle$ is the fluid velocity field in the cell chamber, μ is the dynamic viscosity of the fluid, and p is the hydrodynamic pressure. We note that in the experiments of [23] the characteristic height (from the basal to dorsal surface of the cell) is roughly $d \approx 20$ µm. This is slightly less than the characteristic width of the fluid domain ($2h_0 \approx 40$ µm), and both are significantly less than the length of the fluid domain ($L_x \approx 400$ µm). Therefore, we make a thin gap approximation to the momentum equation of Newtonian fluid [1]. This allows us to reduce the Stokes equation in the x-direction to

$$\mu \frac{\partial^2 u}{\partial z^2} = \frac{\partial p}{\partial x}. \tag{A.3}$$

The lubrication approximation also allows us to claim that p is not a function of z. Therefore, eq. (A.3) is easily solvable. Integrating twice and imposing a no-slip boundary condition on the basal and dorsal surfaces of the fluid domain ($z = \pm d/2$), we solve for the flow profile as a function of z:

$$u(z) = \frac{p_x}{8\mu} \left(d^2 - 4z^2 \right). \tag{A.4}$$

This is simply the standard Poiseuille flow profile [29]. Now, we can utilize this flow profile to evaluate the viscous stress applied by the flow to the basal surface of the cell

$$\sigma = \mu \left. \frac{\partial u}{\partial z} \right|_{z=-\frac{d}{2}} = -\frac{p_x d}{2}. \tag{A.5}$$

Finally, note that most experiments performed on *Physarum* measure the intracellular velocity in the xy-plane. Therefore, we make the simplifying assumption that the experimentally measured velocity can be characterized by the *average* velocity over the height of the cell. We calculate this mean velocity as

$$\bar{u} = \frac{1}{d} \int_{\frac{-d}{2}}^{\frac{d}{2}} u(z)\, dz = \frac{-p_x d^2}{12\mu}. \tag{A.6}$$

For the remainder of this discussion, we will only be concerned with the two-dimensional, planar flow within the cell chamber. Therefore, we will drop the "bar" notation and refer to the mean velocity in the longitudinal direction as u. Similarly, v will denote the average velocity in the lateral (y-) direction. However, this should be understood to imply that the flow has already been averaged over the z-coordinate. We now relate the flux of fluid in the longitudinal direction to the basal viscous stress. The flux Q is defined by

$$Q(x,t) = \int_{-h}^{h} u\, dy. \tag{A.7}$$

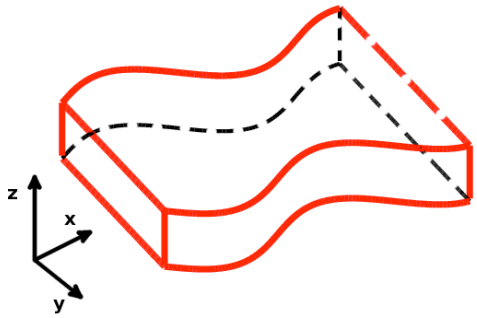

(a) Schematic of the peristaltic chamber.

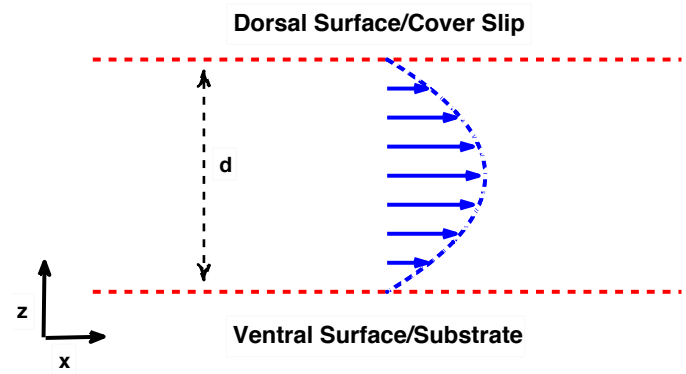

(b) Side view of peristaltic chamber with Poiseille flow profile.

Figure A.1: A schematic of the geometry for our model. The chamber is assumed to be of uniform thickness (d) in the z-direction. The longitudinal flow profile in this direction is assumed to be a parabolic Poiseuille flow.

This quantity does not correspond to the traditional notion of volumetric flux. In our model, Q has units of *area per time*, as opposed to volume per time. However, it is our chosen quantity of interest and will be referred to as "flux" throughout this discussion.

We now directly calculate the flux from the longitudinal fluid velocity u. In order to do this, we make use of our earlier approximations. Since the pressure is assumed to not be a function of y, eq. (A.6) indicates that the velocity u is not either. This leads us to a uniform flow profile in the y-direction. This assumption, coupled with eq. (A.6), leads to

$$u(x,y) = u(x) = \frac{-p_x d^2}{12\mu}. \tag{A.8}$$

Integrating to find the flux immediately gives

$$Q(x) = \int_{-h}^{h} u(x)\, dy = 2hu(x) = \frac{-p_x h d^2}{6\mu}. \tag{A.9}$$

It should be noted that our assumption of uniform flow in the y-direction is not particularly critical to the above relationship. The uniform profile in y is obviously a crude approximation and indeed does not even satisfy a no-slip boundary condition at $y = \pm h$. We *could* perform another lubrication approximation on the two-dimensional flow to account for variations in the y-direction. This would yield that u has a Poiseuille flow profile in the y-direction. If the magnitude of this Poiseuille flow is given by eq. (A.6), then we may write

$$u(x,y) = \frac{-p_x(x) d^2}{12\mu}\left(1 - \left(\frac{y}{h}\right)^2\right). \tag{A.10}$$

Integrating over a chamber cross section gives

$$Q(x) = \int_{-h}^{h} u(x,y)\, dy = \frac{-p_x h d^2}{9\mu}. \tag{A.11}$$

Thus we see that the precise assumption regarding the flow profile in the y-direction is not critical, as its effect on the calculated flux simply amounts to an order one constant. This calculation is

purely expository. For the entirety of this work, we will assume that the flow profile is uniform in the y-direction, and thus the flux $Q(x)$ is given by eq. (A.9). Combining eqs. (A.5) and (A.9), we can relate the flux Q and boundary deformation h to the characteristic viscous stresses associated with the flow

$$\sigma = \frac{3\mu}{d}\frac{Q(x,t)}{h(x,t)}. \tag{A.12}$$

A.1.2 Parameters used for Analytical Model

Table A.1: Model parameters for peristaltic chamber

Symbol	Description	Value
L_x	Cell Length	400 µm
h_0	Average Cell Half-Width	20 µm
A	Deformation Amplitude	5 µm
d	Cell Thickness	20 µm
k	Deformation Wave Number	$\pi/2$
T	Deformation Wave Period	100 sec
μ	Cytosol Viscosity	16.66 Pa sec

All of the parameters were chose to match the data presented in [23], with the exception of one. The viscosity of cytoplasm within *Physarum* plasmodia is not an easily quantifiable mechanical parameter. Indeed, estimates may range over many orders of magnitude depending on experimental procedure and cell preparation. However, our model does provide us a way to crudely estimate cytoplasmic viscosity. Equation (A.8) allows us to perform this estimation, provided that we know the characteristic flow velocity and pressure gradient. While we do not know the local pressure gradient within the cell, we do know the characteristic length of the cell body (L_x). We also have estimates for the characteristic pressure difference ($[p]$) from the anterior to posterior of the cell [14]. Finally, it is relatively easy to extract a characteristic velocity scale from the data in [23]. The additional parameters needed to estimate μ are listed in table A.2.

Table A.2: Parameters used to calculate cytosol viscosity in *Physarum*.

Symbol	Description	Value
$[p]$	Pressure difference across cell	1000 Pa
U	Characteristic fluid velocity	5 µm/sec

Using the values listed in tables A.1 and A.2 and eq. (A.8), we approximate the viscosity of the intracellular fluid as

$$\mu \approx \frac{[p]d^2}{12L_xU}. \tag{A.13}$$

This yields a viscosity of $\mu = 50/3$ Pa sec ≈ 17 Pa sec. For comparison, this is roughly the viscosity of honey, or approximately $17,000$ times the viscosity of water. As previously stated, measuring the viscosity of cytoplasm is a difficult problem, partially due to the ambiguity of the material being measured. Cytoplasm is a complex mixture of ions, proteins, and other compounds. Proteins such as actin may polymerize (to form a gel-like network) or depolymerize spontaneously or in response to various chemical signals. This means that the measured rheology of cytoplasm can vary wildly

depending on timescale of interest, experimental methodology, environmental factors, or cell type [22]. Values for cytoplasmic viscosity have been reported over several orders of magnitude [21], ranging up to 10^4 Pa sec for fibroblasts [43]. Furthermore, our model has homogenized all of this complex rheology into a single parameter. Therefore, while the computed value of μ is rather high to describe *cytosol*, it is well within a reasonable range to describe the viscosity of cytoplasm.

A.2 Computational Model Details

A.2.1 Parameters for Numerical Model

Our mathematical model is based on the Immersed Boundary (IB) method, which was originally developed to simulate blood flow [28], but has since been adopted to address an array of fluid-structure interaction problems in biology and engineering [24]. The key feature of the IB method is that the equations of fluid mechanics are solved in a fixed Eulerian coordinate system (with coordinate $\vec{x}_{\text{lab}}$ and domain Ω), while the equations of the immersed solid structure are represented in a moving Lagrangian coordinate system (with coordinate $\vec{x}$ and domain Γ). The basic framework of our methodology is outlined in [35]. A more detailed explanation for the specific simulations used in this work are provided in [20] and its supplemental material.

In nearly all cases, constitutive equations and parameter values are chosen identical to those used in [20]. Here, we provide values and verbal descriptions of the relevant parameters. The cell boundary is defined by an elastic, impermeable membrane under surface tension. The membrane elastic stiffness is denoted κ and the resting tension is γ. The resting tension γ is chosen to give a resting pressure within the cell of approximately 500 Pa. This value was desired because of evidence that the resting pressure within *Physarum* is of the same scale as traction stresses generated during motility. The elastic stiffness κ was set to be $\gamma/2$ based on micropipette experiments (in other cell types) that show inhibiting cortical myosin reduces membrane/cortex tension response by as much as 50% [44] (see Supplemental Information of [20] for a more detailed discussion of membrane parameters). The resting geometry is a straight channel with two semicircular caps (as depicted in fig. 7). The overall cell length and width are L_x and L_y respectively.

The interior of the cell body is a poroelastic material composed of a permeable elastic network (cytoskeleton) and viscous interstitial fluid (cytosol). The elastic modulus of the cytoskeletal network is denoted λ, while the cytosol has viscosity μ. The strength of drag due to relative motion of cytosol and cytoskeleton is proportional to the parameter ξ. The ratio μ/ξ may be interpreted as the Darcy permeability of the network, and is the important parameter governing the flow of cytosol. We estimate an "effective" Darcy permeability for the cell interior of approximately 33.3 μm^2. This value is calculated by averaging two distinct flow environments over the cross section of the cell. We assume that a cross section of the cell is comprised of a dense actin rich cytoplasmic gel, with a non-gelated flow channel in the center. We assume that the flow channel occupies approximately 25% of the cell cross-sectional width, and exhibits viscous flow governed by Stokes equation. The gelated regions on either side of the flow channel are governed by a Brinkman equation, with a Darcy permeability of 10^{-4} μm^2 [8, 15]. Details of this averaging calculation can be found in [19], as well as the Supplemental Information of [20]. The fluid viscosity is chosen to be well within reported values for cytoplasmic viscosity, which vary wildly depending on cell type and experimental methodology [21]. Once cytoplasmic viscosity has been chosen, the drag parameter ξ is uniquely determined to keep the poroelastic medium consistent with the desired permeability. Non-dimensionalization of the fluid equations shows that the ratio of viscous stresses to drag forces can be characterized by the ratio of the length scale of the cell squared to the Darcy permeability ($\xi L^2/\mu$). Given our estimate of the Darcy permeability, this ratio is much less than 1, indicating

that the fluid dynamics are drag dominated. This implies that our specific choice of fluid viscosity does not affect the physics of the system dramatically.

We drive the simulation by imposing a wave of contractile stress within the network. The strength of contractile stress A_{stress} was chosen to produce cell deformations on the scale observed *in vivo*. The wave number and frequency of the the *contraction* wave in Section 6 were chosen identical to the wave number and frequency of the *deformation* wave in Section 3. We have no data describing the actual contractions within *Physarum* which drive the observed peristaltic deformations. However, in our numerical experiments, choosing these values for k and ω produced peristaltic deformations with phase velocity consistent with experiments. The overall period of the contraction and deformation is given by $T = 2\pi/\omega$ and reported in table A.3.

Finally, the elastic cytoskeleton is mechanically coupled to the substrate via adhesive complexes. We model the interaction of the adhesive complexes via a viscous drag law with a spatiotemporal variation in the viscous drag parameter (eq. (27)). The basal strength of viscous interaction ε represents non-specific interactions between the dorsal surface of the cell and the substrate. The parameter A_{adh} represents the strength of specific interactions between integrin-like ligands in the cell membrane and the substrate. This parameter was varied over many orders of magnitude. We report here only the values that resulted in non-trivial migration speed in simulations. Finally, the phase of adhesion relative to coordination ϕ was chosen based on our previous results reported in [20]. This value results in robust migration which allowed us to investigate the effects of altering the elastic modulus of the cell.

Table A.3: Model parameters for crawling simulation.

Parameter	Description	Numerical Value
L_x	Cell Length	400 µm
L_y	Cell Width	66.6 µm
κ	Cell Membrane Stiffness	10^{-2} N/m
γ	Cell Membrane Resting Tension	6.1×10^{-2} N/m
μ	Cytosol Viscosity	0.75 Pa sec.
λ	Cytoskeletal Elastic Modulus	781 Pa
ξ	Cytosol/Cytoskeletal Drag Coefficient	2.29×10^{11} Pa sec/m^2
A_{stress}	Amplitude of Active Contraction	5.8 Pa
k	Wave Number of Active Contraction	$\pi/2$
T	Period of Active Contraction	100 sec
ϵ	Coefficient of Nonspecific Adhesion	2.29×10^6 Pa sec/m
A_{adh}	Coefficient of Specific Adhesion	2.29×10^6 – 2.29×10^{10} Pa sec/m
ϕ	Relative Phase of Contraction and Specific Adhesion	$3\pi/2$